arXiv:hep-ex/0005018v2   5 Jul 2000

Measurement of the Proton Structure Function F_2 at Very Low Q^2 at HERA

ZEUS Collaboration

Abstract

A measurement of the proton structure function $F_2(x, Q^2)$ is presented in the kinematic range $0.045\,\mathrm{GeV}^2 < Q^2 < 0.65\,\mathrm{GeV}^2$ and $6\cdot10^{-7} < x < 1\cdot10^{-3}$. The results were obtained using a data sample corresponding to an integrated luminosity of $3.9\,\mathrm{pb}^{-1}$ in e^+p reactions recorded with the ZEUS detector at HERA. Information from a silicon-strip tracking detector, installed in front of the small electromagnetic calorimeter used to measure the energy of the final-state positron at small scattering angles, together with an enhanced simulation of the hadronic final state, has permitted the extension of the kinematic range beyond that of previous measurements. The uncertainties in F_2 are typically less than 4%. At the low Q^2 values of the present measurement, the rise of F_2 at low x is slower than observed in HERA data at higher Q^2 and can be described by Regge theory with a constant logarithmic slope $\partial\ln F_2/\partial\ln(1/x)$. The dependence of F_2 on Q^2 is stronger than at higher Q^2 values, approaching, at the lowest Q^2 values of this measurement, a region where F_2 becomes nearly proportional to Q^2.

The ZEUS Collaboration

J. Breitweg, S. Chekanov, M. Derrick, D. Krakauer, S. Magill, B. Musgrave, A. Pellegrino, J. Repond,
R. Stanek, R. Yoshida
Argonne National Laboratory, Argonne, IL, USA [p]

M.C.K. Mattingly
Andrews University, Berrien Springs, MI, USA

G. Abbiendi, F. Anselmo, P. Antonioli, G. Bari, M. Basile, L. Bellagamba, D. Boscherini[1], A. Bruni,
G. Bruni, G. Cara Romeo, G. Castellini[2], L. Cifarelli[3], F. Cindolo, A. Contin, N. Coppola, M. Corradi,
S. De Pasquale, P. Giusti, G. Iacobucci, G. Laurenti, G. Levi, A. Margotti, T. Massam, R. Nania,
F. Palmonari, A. Pesci, A. Polini, G. Sartorelli, Y. Zamora Garcia[4], A. Zichichi
University and INFN Bologna, Bologna, Italy [f]

C. Amelung, A. Bornheim[5], I. Brock, K. Coböken[6], J. Crittenden, R. Deffner[7], H. Hartmann, K. Hein-
loth, E. Hilger, P. Irrgang, H.-P. Jakob, A. Kappes, U.F. Katz, R. Kerger, E. Paul, H. Schnurbusch,
A. Stifutkin, J. Tandler, K.C. Voss, A. Weber, H. Wieber
Physikalisches Institut der Universität Bonn, Bonn, Germany [c]

D.S. Bailey, O. Barret, N.H. Brook[8], B. Foster[9], G.P. Heath, H.F. Heath, J.D. McFall, D. Piccioni,
E. Rodrigues, J. Scott, R.J. Tapper
H.H. Wills Physics Laboratory, University of Bristol, Bristol, U.K. [o]

M. Capua, A. Mastroberardino, M. Schioppa, G. Susinno
Calabria University, Physics Dept.and INFN, Cosenza, Italy [f]

H.Y. Jeoung, J.Y. Kim, J.H. Lee, I.T. Lim, K.J. Ma, M.Y. Pac[10]
Chonnam National University, Kwangju, Korea [h]

A. Caldwell, W. Liu, X. Liu, B. Mellado, S. Paganis, S. Sampson, W.B. Schmidke, F. Sciulli
Columbia University, Nevis Labs., Irvington on Hudson, N.Y., USA [q]

J. Chwastowski, A. Eskreys, J. Figiel, K. Klimek, K. Olkiewicz, K. Piotrzkowski[11], M.B. Przybycień,
P. Stopa, L. Zawiejski
Inst. of Nuclear Physics, Cracow, Poland [j]

B. Bednarek, K. Jeleń, D. Kisielewska, A.M. Kowal, T. Kowalski, M. Przybycień, E. Rulikowska-
Zarębska, L. Suszycki, D. Szuba
Faculty of Physics and Nuclear Techniques, Academy of Mining and Metallurgy, Cracow, Poland [j]

A. Kotański
Jagellonian Univ., Dept. of Physics, Cracow, Poland [k]

L.A.T. Bauerdick, U. Behrens, J.K. Bienlein, C. Burgard[12], D. Dannheim, K. Desler, G. Drews,
A. Fox-Murphy, U. Fricke, F. Goebel, P. Göttlicher, R. Graciani, T. Haas, W. Hain, G.F. Hart-
ner, D. Hasell[13], K. Hebbel, K.F. Johnson[14], M. Kasemann[15], W. Koch, U. Kötz, H. Kowalski,
L. Lindemann[16], B. Löhr, M. Martínez, M. Milite, T. Monteiro[11], M. Moritz, D. Notz, F. Peluc-
chi, M.C. Petrucci, M. Rohde, P.R.B. Saull, A.A. Savin, U. Schneekloth, F. Selonke, M. Sievers[17],
S. Stonjek, E. Tassi, G. Wolf, U. Wollmer, C. Youngman, W. Zeuner
Deutsches Elektronen-Synchrotron DESY, Hamburg, Germany

C. Coldewey, A. Lopez-Duran Viani, A. Meyer, S. Schlenstedt, P.B. Straub
DESY Zeuthen, Zeuthen, Germany

G. Barbagli, E. Gallo, P. Pelfer
University and INFN, Florence, Italy [f]

G. Maccarrone, L. Votano
INFN, Laboratori Nazionali di Frascati, Frascati, Italy [f]

A. Bamberger, A. Benen, S. Eisenhardt[18], P. Markun, H. Raach, S. Wölfle
Fakultät für Physik der Universität Freiburg i.Br., Freiburg i.Br., Germany [c]

P.J. Bussey, M. Bell, A.T. Doyle, S.W. Lee, A. Lupi, N. Macdonald, G.J. McCance, D.H. Saxon,
L.E. Sinclair, I.O. Skillicorn, R. Waugh
Dept. of Physics and Astronomy, University of Glasgow, Glasgow, U.K. [o]

I. Bohnet, N. Gendner, U. Holm, A. Meyer-Larsen, H. Salehi, K. Wick
Hamburg University, I. Institute of Exp. Physics, Hamburg, Germany [c]

A. Garfagnini, I. Gialas[19], L.K. Gladilin[20], D. Kçira[21], R. Klanner, E. Lohrmann, G. Poelz, F. Zetsche
Hamburg University, II. Institute of Exp. Physics, Hamburg, Germany [c]

R. Goncalo, K.R. Long, D.B. Miller, A.D. Tapper, R. Walker
Imperial College London, High Energy Nuclear Physics Group, London, U.K. [o]

U. Mallik
University of Iowa, Physics and Astronomy Dept., Iowa City, USA [p]

P. Cloth, D. Filges
Forschungszentrum Jülich, Institut für Kernphysik, Jülich, Germany

T. Ishii, M. Kuze, K. Nagano, K. Tokushuku[22], S. Yamada, Y. Yamazaki
Institute of Particle and Nuclear Studies, KEK, Tsukuba, Japan [g]

S.H. Ahn, S.B. Lee, S.K. Park
Korea University, Seoul, Korea [h]

H. Lim, I.H. Park, D. Son
Kyungpook National University, Taegu, Korea [h]

F. Barreiro, G. García, C. Glasman[23], O. González, L. Labarga, J. del Peso, I. Redondo[24], J. Terrón
Univer. Autónoma Madrid, Depto de Física Teórica, Madrid, Spain [n]

M. Barbi, F. Corriveau, D.S. Hanna, A. Ochs, S. Padhi, M. Riveline, D.G. Stairs, M. Wing
McGill University, Dept. of Physics, Montréal, Québec, Canada [a], [b]

T. Tsurugai
Meiji Gakuin University, Faculty of General Education, Yokohama, Japan

A. Antonov, V. Bashkirov[25], M. Danilov, B.A. Dolgoshein, D. Gladkov, V. Sosnovtsev, S. Suchkov
Moscow Engineering Physics Institute, Moscow, Russia [l]

R.K. Dementiev, P.F. Ermolov, Yu.A. Golubkov, I.I. Katkov, L.A. Khein, N.A. Korotkova,
I.A. Korzhavina, V.A. Kuzmin, O.Yu. Lukina, A.S. Proskuryakov, L.M. Shcheglova, A.N. Solomin,
N.N. Vlasov, S.A. Zotkin
Moscow State University, Institute of Nuclear Physics, Moscow, Russia [m]

C. Bokel, M. Botje, N. Brümmer, J. Engelen, S. Grijpink, E. Koffeman, P. Kooijman, S. Schagen,
A. van Sighem, H. Tiecke, N. Tuning, J.J. Velthuis, J. Vossebeld, L. Wiggers, E. de Wolf
NIKHEF and University of Amsterdam, Amsterdam, Netherlands [i]

D. Acosta[26], B. Bylsma, L.S. Durkin, J. Gilmore, C.M. Ginsburg, C.L. Kim, T.Y. Ling
Ohio State University, Physics Department, Columbus, Ohio, USA [p]

S. Boogert, A.M. Cooper-Sarkar, R.C.E. Devenish, J. Große-Knetter[27], T. Matsushita, A. Quadt[11], O. Ruske, M.R. Sutton, R. Walczak
Department of Physics, University of Oxford, Oxford U.K. [o]

A. Bertolin, R. Brugnera, R. Carlin, F. Dal Corso, U. Dosselli, S. Dusini, S. Limentani, M. Morandin, M. Posocco, L. Stanco, R. Stroili, M. Turcato, C. Voci
Dipartimento di Fisica dell' Università and INFN, Padova, Italy [f]

L. Adamczyk[28], L. Iannotti[28], B.Y. Oh, J.R. Okrasiński, W.S. Toothacker, J.J. Whitmore
Pennsylvania State University, Dept. of Physics, University Park, PA, USA [q]

Y. Iga
Polytechnic University, Sagamihara, Japan [g]

G. D'Agostini, G. Marini, A. Nigro
Dipartimento di Fisica, Univ. 'La Sapienza' and INFN, Rome, Italy [f]

C. Cormack, J.C. Hart, N.A. McCubbin, T.P. Shah
Rutherford Appleton Laboratory, Chilton, Didcot, Oxon, U.K. [o]

D. Epperson, C. Heusch, H.F.-W. Sadrozinski, A. Seiden, R. Wichmann, D.C. Williams
University of California, Santa Cruz, CA, USA [p]

N. Pavel
Fachbereich Physik der Universität-Gesamthochschule Siegen, Germany [c]

H. Abramowicz[29], S. Dagan[30], S. Kananov[30], A. Kreisel, A. Levy[30]
Raymond and Beverly Sackler Faculty of Exact Sciences, School of Physics, Tel-Aviv University, Tel-Aviv, Israel [e]

T. Abe, T. Fusayasu, K. Umemori, T. Yamashita
Department of Physics, University of Tokyo, Tokyo, Japan [g]

R. Hamatsu, T. Hirose, M. Inuzuka, S. Kitamura[31], T. Nishimura
Tokyo Metropolitan University, Dept. of Physics, Tokyo, Japan [g]

M. Arneodo[32], N. Cartiglia, R. Cirio, M. Costa, M.I. Ferrero, S. Maselli, V. Monaco, C. Peroni, M. Ruspa, R. Sacchi, A. Solano, A. Staiano
Università di Torino, Dipartimento di Fisica Sperimentale and INFN, Torino, Italy [f]

M. Dardo
II Faculty of Sciences, Torino University and INFN - Alessandria, Italy [f]

D.C. Bailey, C.-P. Fagerstroem, R. Galea, T. Koop, G.M. Levman, J.F. Martin, R.S. Orr, S. Polenz, A. Sabetfakhri, D. Simmons
University of Toronto, Dept. of Physics, Toronto, Ont., Canada [a]

J.M. Butterworth, C.D. Catterall, M.E. Hayes, E.A. Heaphy, T.W. Jones, J.B. Lane, B.J. West
University College London, Physics and Astronomy Dept., London, U.K. [o]

J. Ciborowski, R. Ciesielski, G. Grzelak, R.J. Nowak, J.M. Pawlak, R. Pawlak, B. Smalska, T. Tymieniecka, A.K. Wróblewski, J.A. Zakrzewski, A.F. Żarnecki
Warsaw University, Institute of Experimental Physics, Warsaw, Poland [j]

M. Adamus, T. Gadaj
Institute for Nuclear Studies, Warsaw, Poland [j]

O. Deppe, Y. Eisenberg, D. Hochman, U. Karshon[30]
Weizmann Institute, Department of Particle Physics, Rehovot, Israel [d]

W.F. Badgett, D. Chapin, R. Cross, C. Foudas, S. Mattingly, D.D. Reeder, W.H. Smith, A. Vaiciulis[33],
T. Wildschek, M. Wodarczyk
University of Wisconsin, Dept. of Physics, Madison, WI, USA [p]

A. Deshpande, S. Dhawan, V.W. Hughes
Yale University, Department of Physics, New Haven, CT, USA [p]

S. Bhadra, C. Catterall, J.E. Cole, W.R. Frisken, R. Hall-Wilton, M. Khakzad, S. Menary
York University, Dept. of Physics, Toronto, Ont., Canada [a]

[1] now visiting scientist at DESY
[2] also at IROE Florence, Italy
[3] now at Univ. of Salerno and INFN Napoli, Italy
[4] supported by Worldlab, Lausanne, Switzerland
[5] now at CalTech, USA
[6] now at Sparkasse Bonn, Germany
[7] now a self-employed consultant
[8] PPARC Advanced fellow
[9] also at University of Hamburg, Alexander von Humboldt Research Award
[10] now at Dongshin University, Naju, Korea
[11] now at CERN
[12] now at Barclays Capital PLC, London
[13] now at Massachusetts Institute of Technology, Cambridge, MA, USA
[14] visitor from Florida State University
[15] now at Fermilab, Batavia, IL, USA
[16] now at SAP A.G., Walldorf, Germany
[17] now at SuSE GmbH, Nürnberg, Germany
[18] now at University of Edinburgh, Edinburgh, U.K.
[19] visitor of Univ. of Crete, Greece, partially supported by DAAD, Bonn - Kz. A/98/16764
[20] on leave from MSU, supported by the GIF, contract I-0444-176.07/95
[21] supported by DAAD, Bonn - Kz. A/98/12712
[22] also at University of Tokyo
[23] supported by an EC fellowship number ERBFMBICT 972523
[24] supported by the Comunidad Autonoma de Madrid
[25] now at Loma Linda University, Loma Linda, CA, USA
[26] now at University of Florida, Gainesville, FL, USA
[27] supported by the Feodor Lynen Program of the Alexander von Humboldt foundation
[28] partly supported by Tel Aviv University
[29] an Alexander von Humboldt Fellow at University of Hamburg
[30] supported by a MINERVA Fellowship
[31] present address: Tokyo Metropolitan University of Health Sciences, Tokyo 116-8551, Japan
[32] now also at Università del Piemonte Orientale, I-28100 Novara, Italy
[33] now at University of Rochester, Rochester, NY, USA

1 Introduction

A remarkable feature of the proton structure function $F_2(x, Q^2)$ is its rapid rise at low x, observed by the H1 and ZEUS collaborations [1] at HERA. First observed for Q^2 values above $10\,\text{GeV}^2$, the persistence of this rise down to small Q^2 [2–4] challenges our understanding of QCD. In a recent publication [4], the ZEUS collaboration has discussed the transition from deep inelastic scattering to photoproduction. It was found that standard non-perturbative approaches which apply in photoproduction fail to describe the data in the region above $Q^2 = 0.9\,\text{GeV}^2$. Next-to-leading-order QCD fits are successful when taken down to these low Q^2 values. As Q^2 approaches $1\,\text{GeV}^2$, however, these fits yield vanishing gluon densities at low x, while the sea-quark density remains finite. Such a "valence-like" gluon distribution, vanishing as $x \to 0$, seems unnatural even at low Q^2 and has led to much discussion [5]. Precise measurements at low Q^2 are important in elucidating this subject.

This letter presents a measurement of F_2 at low Q^2 ($0.045\,\text{GeV}^2 < Q^2 < 0.65\,\text{GeV}^2$) and low x ($6 \cdot 10^{-7} < x < 1 \cdot 10^{-3}$). The data used correspond to an integrated luminosity of $3.9\,\text{pb}^{-1}$ and were taken with dedicated triggers during six weeks of e^+p running in 1997. Compared to a previous result[1] [2], the new measurement covers a larger kinematic region with an improved statistical precision and systematic accuracy. This was made possible by the addition of a Beam Pipe Tracker in front of the Beam Pipe Calorimeter used for measuring the energy of the final-state positron at small scattering angles, and by an enhanced simulation of the hadronic final state.

2 Kinematic variables and cross sections

Inclusive deep inelastic positron-proton scattering, $e^+p \to e^+X$, can be described in terms of two kinematic variables, x and Q^2, where x is the Bjorken scaling variable and Q^2 the negative of the square of the four-momentum transfer. They are defined as $Q^2 = -q^2 = -(k - k')^2$ and $x = Q^2/(2P \cdot q)$, where k and P are the four-momenta of the incoming positron and proton, respectively, and k' is the four-momentum of the scattered positron. The fractional energy transferred to the proton in its rest frame, y, is related to x and Q^2 by $Q^2 = sxy$, where $s = 4E_eE_p$ is the square of the positron-proton center-of-mass energy. Here, $E_e = 27.5\,\text{GeV}$ and $E_p = 820\,\text{GeV}$ are the positron and proton beam energies, respectively.

At the low Q^2 values of this measurement, where the contribution from Z exchange is negligible, the double-differential cross section for inelastic e^+p scattering can be written in terms of F_2 and the longitudinal structure function F_L as

$$\frac{d^2\sigma}{dx\,dQ^2} = \frac{2\pi\alpha^2}{xQ^4}\left((1 + (1 - y)^2)F_2 - y^2F_L\right)(1 + \delta_r). \tag{1}$$

The QED radiative correction, δ_r, is a function of x and Q^2, but, to a good approximation, independent of both F_2 and F_L [9].

3 Experimental setup and kinematic reconstruction

The ZEUS detector has been described in detail previously [10]. In the present analysis, the scattered positron was detected in the Beam Pipe Calorimeter (BPC) and Beam Pipe Tracker (BPT) [11, 12]. The BPC was installed in 1995 to enhance the acceptance of the ZEUS detector for low-Q^2 events, where the positron is scattered through a small angle, and was used for a previous measurement of F_2 [2]. In 1997, the BPT was installed in front of the BPC to complement the calorimetric energy measurement with precise tracking information.

---

[1] When the previous measurement of F_2 at low Q^2 was published, it was found that existing models and parameterizations [6] were unable to describe the data. Subsequently, there have been various new approaches, as well as updates and improvements of existing ones, to describe $F_2(x, Q^2)$ in the entire Q^2 range [7, 8]. The validity of these recent models is not discussed here.

3.1 Beam Pipe Calorimeter and Beam Pipe Tracker

The BPC is a tungsten-scintillator sampling calorimeter with the front face located at $Z = -293.7\,\text{cm}$, the center at $Y = 0.0\,\text{cm}$, and the inner edge of the active area at $X = 4.4\,\text{cm}$, as close as possible to the rear beam pipe[2]. The BPC has an active area of $12.0 \times 12.8\,\text{cm}^2$ in $X \times Y$ and its depth in Z corresponds to $24\,X_0$. The relative energy resolution as determined in test-beam measurements with 1–6 GeV electrons is $\Delta E/E = 17\%/\sqrt{E\,[\text{GeV}]}$. The scintillator layers are alternately subdivided into vertical and horizontal strips, 7.9 mm in width, referred to as X and Y fingers, respectively. The stacks of fingers with common X and Y positions are read out together by a wavelength shifter bar.

The BPT is a silicon microstrip tracking device. In 1997, it was equipped with two detector planes to measure the X coordinate. The planes, of dimensions $6 \times 6 \times 0.03\,\text{cm}^3$, have 576 strips with a $100\,\mu\text{m}$ pitch. The detectors are read out with binary electronics [13]. The number of readout channels per detector is 512; 128 strips at the outer edge of a plane are read out in pairs, thus giving an effective pitch of $200\,\mu\text{m}$. The detector planes and front-end electronics are supported in a carbon-fiber composite structure attached to the front face of the BPC. The planes are positioned at $Z = -252.7\,\text{cm}$ and $Z = -279.1\,\text{cm}$ and have centers at $X = 6.85\,\text{cm}$ and $Y = 0.0\,\text{cm}$.

Scattered positrons traveling from the interaction point toward the BPC and BPT leave the beam pipe through a 1.5 mm thick $(1.6\%\,X_0)$ aluminum exit window positioned at $Z = -249.8\,\text{cm}$. The fiducial area of the measurement was defined by the overlap of the exit window with the acceptance of BPC and BPT, and was thus limited to a D-shaped region in the range $5.2\,\text{cm} < X < 9.3\,\text{cm}$ and $-2.3\,\text{cm} < Y < 2.8\,\text{cm}$ at $Z = -293.7\,\text{cm}$. Only positrons scattered into the fiducial area were used in the analysis, yielding an angular acceptance of $18\,\text{mrad} < \theta_e < 32\,\text{mrad}$ for particles emanating from the nominal interaction point.

3.2 Measurement of the scattered positron

The combination of calorimetric and tracking information for the measurement of the four-momentum of the scattered positron resulted in significant improvements with respect to the previous analysis. The BPT tracking information proved crucial in suppressing beam- and neutral-particle-related backgrounds. It also allowed a better control of the systematic uncertainties in the position-dependent corrections to the BPC energy measurement, the development of an improved position reconstruction algorithm for the BPC, a direct determination of the fiducial area of the measurement, and a significant reduction of the uncertainty in the position of the BPC. Moreover, the fact that the longitudinal coordinate of the event vertex was reconstructed from the scattered-positron track reduced the dependence of the reconstruction of kinematic variables on the hadronic final state.

The energy deposited in the BPC by the scattered positron was reconstructed as the sum over all energies measured in the BPC fingers. Calibration constants for individual stacks of fingers were determined using kinematic-peak events[3], taking into account position-dependent corrections for transverse shower leakage from the BPC, light attenuation in the scintillator fingers, and the non-uniformity caused by the gaps between fingers [12]. After the calibration procedure, the BPC energy response was found to be uniform to within 0.3%, and the absolute energy scale at 27.5 GeV was known to 0.3%. The linearity of the energy response was estimated through a simulation based on the results of a scan with a ^{60}Co source; it was found that the energy scale at 4 GeV was accurate to within 1% [14]. The results of the simulation were confirmed by a study of QED Compton scattering events [15].

The transverse position of a positron shower in the BPC was reconstructed by using the correlation between the shower position relative to the center of the struck stack of BPC fingers and the energy

---

[2]The ZEUS right-handed Cartesian coordinate system has its origin at the nominal interaction point, the Z axis pointing in the proton beam direction (referred to as forward direction), and the X axis pointing toward the center of HERA. The polar angle ϑ is measured with respect to the positive Z axis; it is convenient to also define $\theta = \pi - \vartheta$. The pseudorapidity is defined as $\eta = -\ln(\tan(\vartheta/2))$.

[3]A cut $y_{\text{JB}} < 0.04$ (see Section 3.3) selects events for which the energy of the scattered positron sharply peaks within 2% of the beam energy, providing a good calibration source (kinematic-peak events).

deposited in its two neighbors. The function correlating the distribution of energy to the shower position was determined by comparing positron positions reconstructed separately with the BPC and the BPT, respectively [12]. The resulting average BPC position resolution was $\Delta X = \Delta Y = 0.22\,\mathrm{cm}/\sqrt{E\,[\mathrm{GeV}]}$.

The projection of the positron scattering angle on the X-Z plane, θ_X, the positron impact point on the BPC front face in X, and the longitudinal position of the event vertex, Z_{vtx}, were determined by reconstructing a BPT track as the straight line joining the hits in the two planes and assuming the average value for the X coordinate of the event vertex, determined with the Central Tracking Detector (CTD, see below). A study of simulated events showed that the effect of the magnetic field was negligible. The value of θ_Y could only be reconstructed from the shower position in the BPC. However, since for positrons scattered into the fiducial area θ_X was significantly larger than θ_Y, the impact of the limited θ_Y resolution on the reconstruction of $\theta_e = \sqrt{\theta_X^2 + \theta_Y^2}$ was small. On average, the angular resolution was $\Delta\theta_e = 0.2\,\mathrm{mrad}$, and the vertex resolution was $\Delta Z_{\mathrm{vtx}} = 3\,\mathrm{cm}$.

The X positions of the BPC and BPT were determined with a minimization procedure based on the comparison between the event vertex reconstructed from the BPC and BPT information and that reconstructed from the CTD tracking information [12]. Several studies were performed to determine the stability of the result: the largest contribution to the systematic error comes from the uncertainty in the relative Z position of the BPT planes, estimated from a survey to be $300\,\mu\mathrm{m}$. The resulting total accuracy in the X positions of the BPC and BPT is $200\,\mu\mathrm{m}$. The tracking efficiency of the BPT was $90.4 \pm 1.5\%$, the inefficiency being primarily due to dead strips.

3.3 Measurement of the hadronic final state

The hadronic final state was measured using the uranium-scintillator calorimeter (CAL) and the CTD. The CAL covers 99.7% of the total solid angle. Under test-beam conditions, its relative energy resolution is $\Delta E/E = 18\%/\sqrt{E\,[\mathrm{GeV}]}$ for electromagnetic showers and $\Delta E/E = 35\%/\sqrt{E\,[\mathrm{GeV}]}$ for hadronic showers. The CTD operates in a $1.43\,\mathrm{T}$ solenoidal magnetic field, and has a relative resolution for full-length tracks of $\Delta p_T/p_T = 0.0058 \cdot p_T \oplus 0.0065 \oplus 0.0014/p_T$, with p_T measured in GeV (the symbol $\oplus$ denotes addition in quadrature). The interaction vertex is measured with a typical resolution along (transverse to) the beam direction of $4\,\mathrm{mm}$ ($1\,\mathrm{mm}$).

Global variables characterizing the hadronic final state were measured by summing all reconstructed hadronic final-state objects. A combination of clusters of energy deposits in the CAL and the corresponding tracks measured in the CTD [16] was found to provide the best resolution in determining the quantities

$$p_X^{\mathrm{had}} = \sum_i E_i \sin\vartheta_i \cos\phi_i, \qquad p_Y^{\mathrm{had}} = \sum_i E_i \sin\vartheta_i \sin\phi_i, \qquad p_Z^{\mathrm{had}} = \sum_i E_i \cos\vartheta_i,$$

$$E^{\mathrm{had}} = \sum_i E_i, \qquad p_T^{\mathrm{had}} = \sqrt{\left(p_X^{\mathrm{had}}\right)^2 + \left(p_Y^{\mathrm{had}}\right)^2}, \qquad \delta^{\mathrm{had}} = E^{\mathrm{had}} - p_Z^{\mathrm{had}}, \qquad y_{\mathrm{JB}} = \frac{\delta^{\mathrm{had}}}{2E_e}. \tag{2}$$

3.4 Kinematic reconstruction

Two methods have been used for the reconstruction of the kinematic variables Q^2 and y; the variable x was then determined from $x = Q^2/(sy)$. The first method uses the energy, E'_e, and angle, θ_e, of the scattered positron ("electron method") to determine

$$Q_e^2 = 2E_e E'_e (1 + \cos\vartheta_e) \approx E_e E'_e \theta_e^2,$$

$$y_e = 1 - \frac{E'_e}{2E_e}(1 - \cos\vartheta_e) \approx 1 - \frac{E'_e}{E_e}. \tag{3}$$

The second method is used for low values of y, where the y resolution of the electron method can be improved by combining the scattered-positron variables with hadronic final-state variables ("$e\Sigma$

method" [17]) to determine

$$Q^2_{e\Sigma} = Q^2_e,$$

$$y_{e\Sigma} = \frac{2E_e}{\delta} \cdot \frac{\delta^{\text{had}}}{\delta},$$

(4)

where δ is defined as $\delta = \delta^{\text{had}} + E'_e(1 - \cos\vartheta_e)$. Four-momentum conservation requires $\delta = 2E_e$ for fully contained and perfectly measured events.

In the analysis, the kinematic variables of the events were reconstructed with the electron method for $y_e > 0.08$, and with the $e\Sigma$ method for $y_{e\Sigma} < 0.08$. The resulting relative resolution in y ranged from about 5% at high y to 25% at low y. The relative Q^2 resolution was about 10% in the entire kinematic range of the present measurement. The use of the $e\Sigma$ method allowed the extension of the measured kinematic range to y values as low as 0.005.

3.5 Luminosity measurement

The luminosity was measured from the rate of photons from the Bethe-Heitler process, $ep \to ep\gamma$, using a lead-scintillator calorimeter [18] positioned at $Z = -107$ m to detect photons scattered through angles of less than 0.5 mrad. The data set used in the analysis corresponded to an integrated luminosity of $3.9\,\text{pb}^{-1}$, with an uncertainty of 1.8%.

4 Trigger, event selection and background

The event selection was based mainly on the requirement of a well-reconstructed positron in the BPC and in the BPT, while additional cuts on the hadronic final state suppressed background and limited effects of resolution smearing (event migrations) and radiative corrections.

Events were selected online by the ZEUS three-level trigger system. The trigger required a minimum energy deposit in the BPC, a timing compatible with an ep interaction, and imposed requirements on energy deposits from the hadronic final state in the CAL. No BPT information was used in the trigger.

The offline event selection imposed tighter requirements than those applied in the trigger. Using an independently triggered control sample, the trigger was found to be more than 99.5% efficient for events passing the offline cuts.

The scattered positron was required to have an energy, E'_e, of at least 4.4 GeV for events reconstructed with the electron method, or at least 20 GeV for the $e\Sigma$ method. The positron position at the BPC front face as extrapolated from the BPT measurement had to lie within the fiducial area. In order to identify electromagnetic showers and reject hadrons, the transverse size (energy-weighted r.m.s.) of the shower in the BPC was required to be less than 0.8 cm. In order to limit migrations from low y, a cut $y_{\text{JB}} > 0.06$ was applied for events reconstructed with the electron method ($y_{\text{JB}} > 0.004$ for the $e\Sigma$ method).

Background came primarily from events in which a particle from the hadronic final state, usually a photon from the decay of a π^0, produced an electromagnetic shower in the BPC, while the scattered positron escaped undetected. Such events originated mostly from photoproduction (with Q^2 lower than measured in the present analysis). In addition, photons from initial- and final-state radiation (ISR and FSR) could produce an electromagnetic shower in the BPC. Since the longitudinal momentum carried away by the undetected particles (usually escaping through the rear beam-pipe hole) decreases δ, a cut $\delta > 30$ GeV was applied to reject both photoproduction background and radiative events with a hard initial-state photon. In addition, background from neutral particles was suppressed through the requirement that the extrapolated track from the BPT match the position of the BPC shower in X within five times the average BPC position resolution. The remaining contamination was determined from the number of events in which the scattered positron was detected in an electromagnetic calorimeter positioned at $Z = -35$ m, designed to tag positrons with $Q^2 < 0.01\,\text{GeV}^2$ scattered

through very low angles, scaled by the calorimeter tagging efficiency (estimated using a sample of simulated photoproduction events passing all selection cuts). The background contamination was found to be less than 1.5% at high y and negligible at low y, and was statistically subtracted from the data sample. The uncertainty associated with this background correction was estimated by comparing it to the number of simulated photoproduction events (in a luminosity-normalized sample) which passed all analysis cuts and taking the difference to be the uncertainty.

In order to suppress beam-related background, the longitudinal coordinate of the event vertex as reconstructed by the BPT was required to lie within 90 cm of the nominal interaction point. A cut $\delta < 65$ GeV rejected events from processes other than ep interactions. The fraction of such background events, determined from events recorded at times when there was no ep beam crossing, was found to be below 0.5% and was neglected.

5   Analysis

5.1   Monte Carlo simulation

Monte Carlo (MC) simulations were used to characterize the accuracy of the kinematic reconstruction, to determine the efficiency of selecting events, to estimate the background rate, and to extract F_2. Non-diffractive processes including first-order QED radiative corrections were simulated using the HERACLES 4.6.1 program with the DJANGOH 1.1 interface [19] to the QCD programs. The program RAPGAP 2.06 [20] was used to simulate diffractive processes in which the incoming proton emits a Pomeron that has partonic structure. The color-dipole model of ARIADNE 4.08 [21] was used for the simulation of the parton shower, while the hadronization was based on the Lund string model of JETSET 7.410 [22]. Photoproduction background events were simulated using PYTHIA 5.724 [23]. All generated events were passed through a detector simulation based on GEANT 3.13 [24].

In order to improve the simulation of the hadronic final state, the diffractive and non-diffractive samples were mixed in a proportion determined from the data (while maintaining a fixed overall MC normalization). This was crucial at high y and low Q^2, where the trigger and offline event selection efficiencies for diffractive and non-diffractive events were significantly different, owing to the different topologies of the hadronic final state. The mixing ratio was determined by optimizing the agreement between data and MC in distributions of hadronic final-state quantities according to a least-squares minimization procedure applied to histograms of these quantities [12]. The hadronic variables chosen for the determination of the mixing ratio, parameterized[4] as a function of x, were the pseudorapidity of the most forward hadronic energy deposit or track, $\eta_{\max}$, and the variables δ^{had} and p_T^{had} in combination. The average of the two results for the mixing fraction was used for the extraction of F_2, while the difference between them was taken into account as a contribution to the systematic uncertainties (see Section 5.4). The fraction of diffractive events used for the extraction of F_2 varied between 10% and 25% over the x range of the measurement.

Figure 1 shows comparisons between distributions of reconstructed positron and hadronic final-state variables in data and simulation for $0.06 < y_{\mathrm{JB}}$ and $y_e < 0.74$. Figure 2a–c shows comparisons between distributions of reconstructed kinematic variables. Good agreement between data and simulation was obtained in this region and the agreement is of similar quality in the remaining kinematic region used for the extraction of F_2.

5.2   Binning of the data

Figure 2d shows the bin boundary grid used to extract F_2. The bin widths in y are approximately three times the y resolution at low y, and twice the resolution at higher y. The bin widths in Q^2 are

---

[4]Although in principle the mixing ratio between the diffractive and non-diffractive Monte Carlo samples may depend on both x and Q^2, it was found that it could be parameterized with sufficient accuracy as a function of x only.

about four times the Q^2 resolution. In the region of overlap, the bin boundaries were chosen to be identical to those used in the previous measurement [2].

The geometrical acceptance (defined as the fraction of events where the scattered positron hits the fiducial area) was determined from the Monte Carlo simulation to be between 4% and 14% for most of the bins, decreasing to 1% for a few bins. The acceptance (defined as the fraction of events passing all selection cuts and generated in a bin that were also reconstructed in that bin) varied between 50% and 70%, and the purity (defined as the fraction of events passing all selection cuts and reconstructed in a bin that were also generated in that bin) typically ranged from 40% to 65%, decreasing to 30% at the lowest y.

5.3 Extraction of F_2

The proton structure function F_2 was measured using an iterative bin-by-bin unfolding method. The measured value of F_2 at a given point (x, Q^2) inside a bin was obtained as the ratio of the numbers of events reconstructed in the bin in data and MC, multiplied by the corresponding F_2 value of the parameterization used in the MC sample. The point (x, Q^2) at which F_2 is quoted was chosen such that y and Q^2 are round numbers close to the center of the bin.

First-order QED radiative corrections were included in the MC simulation used for the unfolding. The uncertainty in these corrections is due principally to the uncertainty in F_2 at x and Q^2 values outside the region of this measurement, which was estimated to be 6% from an analysis of events with ISR [12] and was taken into account in the systematic error calculation. Higher-order QED radiative corrections, including soft-photon exponentiation, were evaluated using the program HECTOR [25] in the leading-log approximation. They were found to be less than 0.2% and were thus neglected.

Since the bin-by-bin unfolding requires a precise simulation of migration effects, which in turn requires F_2 to be approximately the same in data and MC, the MC sample was iteratively re-weighted by the extracted F_2. The contribution from F_L was neglected in this procedure. The MC events were weighted according to the ALLM97 [7] parameterization in the first iteration, and according to a function of the form[5] [4]

$$F_2(x, Q^2) = \left(\frac{Q^2}{4\pi^2 \alpha} \right) \cdot \left(\frac{M_0^2}{M_0^2 + Q^2} \right) \cdot \left(A_{\mathbb{R}} \cdot \left(\frac{Q^2}{x} \right)^{\alpha_{\mathbb{R}} - 1} + A_{\mathbb{P}} \cdot \left(\frac{Q^2}{x} \right)^{\alpha_{\mathbb{P}} - 1} \right) \tag{5}$$

in further steps. At each iteration, $\alpha_{\mathbb{R}}$ was fixed to the value 0.5 and the values of the remaining four parameters in Eq. (5) were obtained from a fit to the results obtained in the previous step; in order to constrain the fit at high x, photoproduction data [28] were also included[6]. The F_2 results converged after a few iterations.

To correct for the effect of F_L, the value of $R = F_L/(F_2 - F_L)$ from the BKS model [29] was used, which, in the range of interest here, can be parameterized to a very good approximation by $R = 0.165 \cdot Q^2/m_\rho^2$, where $m_\rho = 0.77 \, \text{GeV}$ is the ρ meson mass. This changed the extracted F_2 in the bins of the present measurement by at most 3% with respect to the values determined assuming $F_L = 0$.

5.4 Systematic uncertainties

The systematic uncertainties in the measured F_2 values were determined by studying the stability of the results under variations of the reconstruction parameters entering detector calibration and

---

[5]This phenomenological parameterization is based on the combination of a simplified version of the generalized vector meson dominance model [26] for the description of the Q^2 dependence and Regge theory [27] for the description of the x dependence of F_2.

[6]For this purpose, Eq. (5) was re-written using $\sigma_{\text{tot}}^{\gamma^* p} = (4\pi^2 \alpha/Q^2) F_2$ and $W^2 = Q^2/x$, where W denotes the photon-proton center-of-mass energy.

alignment, of the simulated detector efficiency, of the event selection cuts, and of several other aspects of the analysis procedure. The reconstruction parameters were varied within their uncertainties. The variations of the selection cuts took into account the degree of arbitrariness in the cut values. The following checks were performed (the effect on F_2 is given in parentheses):

- Analysis cuts:

  - variation of the cut $\delta > 30\,\text{GeV}$ by $\pm 2\,\text{GeV}$ (mostly below 1.5%, up to 4% at high y);
  - variation of the cut $y_{\text{JB}} > 0.06$ by ± 0.01, and of the cut $y_{\text{JB}} > 0.004$ by ± 0.001 (up to 1.5% at medium y);
  - variation of the BPC shower-width cut at $0.8\,\text{cm}$ by $\pm 0.1\,\text{cm}$ (up to 1.5% at low positron energies);
  - variation of the 5σ BPC shower/BPT track-match cut by $\pm 2\sigma$ (up to 1.5% at low positron energies);
  - change of the BPT vertex cut from $\pm 90\,\text{cm}$ to $\pm 50\,\text{cm}$ (up to 3.5% in bins with low geometrical acceptance);
  - variation of the fiducial cut in X by $\pm 1\,\text{mm}$ (mostly below 1.5%, up to 6% in bins with low geometrical acceptance);
  - variation of the fiducial cut in Y by $\pm 1\,\text{mm}$ (up to 2.5%).

- Detector calibration, alignment, and efficiency:

  - variation of the BPC energy scale by $\pm 0.3\%$ (up to 2.5% at low y);
  - variation of the BPC energy response by $\pm 1\%$ at $4\,\text{GeV}$, decreasing linearly to 0% at $27.5\,\text{GeV}$ (up to 2.5% at medium and high y);
  - variation of the absolute BPC/BPT position in X by $\pm 200\,\mu\text{m}$ (mostly 1.5%, up to 3.5% in some bins);
  - variation of the simulated BPT efficiency by $\pm 1.5\%$ (1.5%);
  - variation of the CAL energy scale for hadrons by $\pm 3\%$ (up to 2.5% at high and low y).

- Analysis procedure:

  - variation of the fractions of DJANGO and RAPGAP events in the MC sample by half of the difference between fractions obtained from separate optimizations in η_{max} or in δ^{had} and p_T^{had} (mostly below 1%, up to 8% in the two highest y bins);
  - variation of the subtracted photoproduction background by $+200\%$ and -100% (up to 2.5% at high y);
  - re-weighting of F_2 in the MC sample, outside the bins used for the measurement, by $\pm 6\%$, which induces a variation of the number of events migrating into the measurement region[7] (up to 3% in some bins).

The total systematic error was computed as the quadratic sum of the individual contributions, separately for positive and negative deviations. The average statistical error is 2.6% and the average systematic error 3.3%. In most bins, the systematic error has a magnitude similar to that of the statistical error. No individual contribution to the systematic error dominates, except in the two highest y bins, where the error is dominated by the uncertainty in the fraction of diffractive events. An additional overall normalization uncertainty of 1.8% due to the luminosity measurement is not included in the systematic error.

---

[7]This check is particularly sensitive to the magnitude of radiative corrections due to migrations of unrecognized ISR events from higher x and lower Q^2, but also to the amount of migrations due to detector resolution effects.

6 Results

The measurement of F_2 presented here uses data in the kinematic region $0.04\,\mathrm{GeV}^2 < Q^2 < 0.74\,\mathrm{GeV}^2$ and $5.3 \cdot 10^{-7} < x < 1.6 \cdot 10^{-3}$, corresponding to $0.005 < y < 0.84$. The values of F_2 extracted in 70 bins are listed in Table 1. Figure 3 shows these F_2 values as a function of x for different bins of Q^2, together with previous ZEUS and H1 data at low Q^2 [2–4] and with data at higher x from the fixed-target experiment E665 [30]. The curve denoted as "ZEUS Regge fit" represents the parameterization of Eq. (5), with the values of the parameters resulting from the last iteration in the extraction of F_2: $A_{\mathbb{R}} = 147.8 \pm 4.6\,\mu\mathrm{b}$, $\alpha_{\mathbb{R}} = 0.5$, $A_{\mathbb{P}} = 62.0 \pm 2.3\,\mu\mathrm{b}$, $\alpha_{\mathbb{P}} = 1.102 \pm 0.007$, $M_0^2 = 0.52 \pm 0.04\,\mathrm{GeV}^2$ (statistical and systematic errors added in quadrature). These results are in good agreement with those previously obtained [4].

The errors in F_2 are significantly reduced compared to the previous measurement [2]. While in general good agreement is observed in the region of overlap, the present results are slightly lower than the previous ones at the lowest Q^2 and low x. At the highest x of this measurement, the present data overlap with data from E665. Although the F_2 values do not differ significantly in the region of overlap, if the ZEUS Regge fit is extrapolated to higher x into the E665 region, it is found to lie about 15% above the E665 values.

The rise of the proton structure function F_2 at low x, observed to be steep in HERA data at higher Q^2, persists down to small Q^2, but becomes shallower as Q^2 decreases into the range of the present measurement. At the low Q^2 values of this measurement, the rise of F_2 at low x is well described by Regge theory assuming a constant logarithmic slope $\partial \ln F_2 / \partial \ln(1/x)$, as reflected in the good agreement between the data and the ZEUS Regge fit.

Figure 4 shows F_2 as a function of Q^2 for different bins of y, together with previous ZEUS and H1 data [1, 3, 4]. At higher Q^2, F_2 is roughly independent of Q^2. The curve denoted as "ZEUS QCD fit" [4] illustrates that this behavior is well described by next-to-leading-order QCD fits down to Q^2 values of about $1\,\mathrm{GeV}^2$. On the other hand, it is clear that F_2 must acquire a stronger Q^2-dependence at sufficiently low Q^2, since conservation of the electromagnetic current requires F_2 to vanish like Q^2 as $Q^2 \to 0$. Dynamical mechanisms, e.g. parton saturation at small x values [31], can produce such a behavior at low Q^2. The present data exhibit a smooth transition to a stronger Q^2 dependence in the Q^2 range between $0.1\,\mathrm{GeV}^2$ and $1\,\mathrm{GeV}^2$, approaching, at the lowest Q^2 values of this measurement, a region where F_2 becomes nearly proportional to Q^2. This transition is well described by the ZEUS Regge fit.

7 Summary

The proton structure function $F_2(x, Q^2)$ has been measured in the kinematic range $0.045\,\mathrm{GeV}^2 < Q^2 < 0.65\,\mathrm{GeV}^2$ and $6 \cdot 10^{-7} < x < 1 \cdot 10^{-3}$, using an e^+p data sample corresponding to an integrated luminosity of $3.9\,\mathrm{pb}^{-1}$. The addition of a Beam Pipe Tracker in front of the Beam Pipe Calorimeter and an enhanced simulation of the hadronic final state have resulted in coverage of a larger kinematic region and in improved statistical precision and systematic accuracy compared to previous results obtained with the Beam Pipe Calorimeter alone.

At the low Q^2 values of the present measurement, the proton structure function F_2 rises more slowly with x than observed in HERA data at higher Q^2. This slow rise can be described by Regge theory with a constant logarithmic slope $\partial \ln F_2 / \partial \ln(1/x)$. Furthermore, the F_2 data presented here exhibit a stronger Q^2 dependence than observed at higher Q^2, approaching, at the lowest Q^2 values of this measurement, a region where F_2 becomes nearly proportional to Q^2.

Acknowledgments

References

[1] ZEUS Collaboration, M. Derrick et al., Z. Phys. **C 72** (1996) 399;
    H1 Collaboration, S. Aid et al., Nucl. Phys. **B 470** (1996) 4.

[2] ZEUS Collaboration, J. Breitweg et al., Phys. Lett. **B 407** (1997) 432.

[3] H1 Collaboration, C. Adloff et al., Nucl. Phys. **B 497** (1997) 3.

[4] ZEUS Collaboration, J. Breitweg et al., Eur. Phys. J. **C 7** (1999) 609.

[5] See e.g. A.H. Mueller, in: Proceedings of the 6th Int. Workshop on DIS and QCD,
    ed. Gh. Coremans and R. Roosen, World Scientific, Singapore (1998);
    R.G. Roberts, Eur. Phys. J. **C 10** (1999) 697, and references therein.

[6] H. Abramowicz et al., Phys. Lett. **B 269** (1991) 465;
    B. Badełek and J. Kwieciński, Phys. Lett. **B 295** (1992) 263;
    A. Capella et al., Phys. Lett. **B 337** (1994) 358;
    A. Donnachie and P.V. Landshoff, Z. Phys. **C 61** (1994) 139.

[7] H. Abramowicz and A. Levy, DESY Report 97-251.

[8] K. Adel, F. Barreiro and F.J. Ynduráin, Nucl. Phys. **B 495** (1997) 221;
    A.B. Kaidalov and C. Merino, Eur. Phys. J. **C 10** (1999) 153;
    A. Donnachie and P.V. Landshoff, Phys. Lett. **B 437** (1998) 408;
    P. Desgrolard, A. Lengyel and E. Martynov, Eur. Phys. J. **C 7** (1999) 655;
    K. Golec-Biernat and M. Wüsthoff, Phys. Rev. **D 59** (1999) 014017;
    E. Gotsman et al., Nucl. Phys. **B 539** (1999) 535;
    D. Haidt, Nucl. Phys. **B** (Proc. Suppl.) **79** (1999) 186;
    A.D. Martin, M.G. Ryskin and A.M. Staśto, Eur. Phys. J. **C 7** (1999) 643;
    D. Schildknecht and H. Spiesberger, BI-TP 97/25.

[9] A. Akhundov et al., Fortsch. Phys. **44** (1996) 373.

[10] The ZEUS Detector, Status Report, DESY (1993).

[11] The ZEUS Beam Pipe Calorimeter and Tracker, to be submitted to Nucl. Instr. Methods;
     T. Monteiro, Doctoral thesis, Hamburg University (1998), DESY-THESIS-1998-027;
     B. Surrow, Doctoral thesis, Hamburg University (1998), DESY-THESIS-1998-004;
     J. Tickner, Doctoral thesis, Oxford University (1997), RAL-TH-97-018.

[12] C. Amelung, Doctoral thesis, Bonn University (1999), BONN-IR-99-14 and
     DESY-THESIS-2000-002.

[13] E. Barberis et al., Nucl. Instr. Methods **A 364** (1995) 507.

[14] I. Bohnet, Doctoral thesis, Hamburg University (1999), DESY-THESIS-1999-041;
U. Fricke, Doctoral thesis, Hamburg University (1999), DESY-THESIS-1999-043.

[15] V. Monaco, Doctoral thesis, Torino University (1998).

[16] ZEUS Collaboration, J. Breitweg et al., Eur. Phys. J. **C 1** (1998) 81;
G. Briskin, Doctoral thesis, University of Tel Aviv (1998), DESY-THESIS-1998-036.

[17] U. Bassler and G. Bernardi, Nucl. Instr. Methods **A 426** (1999) 583.

[18] ZEUS Collaboration, M. Derrick et al., Z. Phys. **C 63** (1994) 391;
J. Andruszków et al., DESY Report 92-066.

[19] A. Kwiatkowski, H. Spiesberger and H.-J. Möhring, Comp. Phys. Comm. **69** (1992) 155;
K. Charchuła, G.A. Schuler and H. Spiesberger, Comp. Phys. Comm. **81** (1994) 381;
`http://www.desy.de/~hspiesb/djangoh.html`.

[20] H. Jung, Comp. Phys. Comm. **86** (1995) 147;
`http://www-h1.desy.de/~jung/rapgap.html`.

[21] L. Lönnblad, Comp. Phys. Comm. **71** (1992) 15.

[22] T. Sjöstrand, Comp. Phys. Comm. **39** (1986) 347 and Comp. Phys. Comm. **82** (1994) 74;
T. Sjöstrand and M. Bengtsson, Comp. Phys. Comm. **43** (1987) 367.

[23] H.U. Bengtsson and T. Sjöstrand, Comp. Phys. Comm. **46** (1987) 43.

[24] R. Brun et al., GEANT 3.13, CERN Report DD/EE/84-1.

[25] A. Arbuzov et al., Comp. Phys. Comm. **94** (1996) 128.

[26] J.J. Sakurai and D. Schildknecht, Phys. Lett. **B 40** (1972) 121.

[27] P.D.B. Collins, *An Introduction to Regge Theory and High Energy Scattering*,
Cambridge University Press (1977).

[28] D.O. Caldwell et al., Phys. Rev. Lett. **40** (1978) 1222;
S.I. Alekhin et al., CERN Report HERA 87-01.

[29] B. Badełek, J. Kwieciński and A. Staśto, Z. Phys. **C 74** (1997) 297.

[30] E665 Collaboration, M.R. Adams et al., Phys. Rev. **D 54** (1996) 3006.

[31] See e.g. K. Golec-Biernat and M. Wüsthoff, Phys. Rev. **D 59** (1999) 014017, and references therein.

Table 1: Measured $F_2(x, Q^2)$ values with statistical and systematic errors. The effect of F_L has been corrected using R from an approximation of the BKS model, $R = 0.165 \cdot Q^2/m_\rho^2$.

Q^2 (GeV^2)	x	y	F_2	$\pm$ stat	$+$ sys	$-$ sys
0.045	$6.21 \cdot 10^{-7}$	0.800	0.0749	0.0039	0.0072	0.0059
0.065	$1.02 \cdot 10^{-6}$	0.700	0.1060	0.0051	0.0076	0.0071
0.065	$8.97 \cdot 10^{-7}$	0.800	0.1043	0.0032	0.0077	0.0077
0.085	$1.56 \cdot 10^{-6}$	0.600	0.1250	0.0060	0.0075	0.0070
0.085	$1.34 \cdot 10^{-6}$	0.700	0.1255	0.0029	0.0055	0.0061
0.085	$1.17 \cdot 10^{-6}$	0.800	0.1289	0.0039	0.0083	0.0081
0.110	$2.43 \cdot 10^{-6}$	0.500	0.1489	0.0056	0.0108	0.0053
0.110	$2.02 \cdot 10^{-6}$	0.600	0.1530	0.0033	0.0053	0.0047
0.110	$1.73 \cdot 10^{-6}$	0.700	0.1569	0.0033	0.0059	0.0065
0.110	$1.51 \cdot 10^{-6}$	0.800	0.1565	0.0056	0.0095	0.0102
0.150	$5.02 \cdot 10^{-6}$	0.330	0.1844	0.0070	0.0078	0.0074
0.150	$4.14 \cdot 10^{-6}$	0.400	0.1880	0.0046	0.0057	0.0041
0.150	$3.31 \cdot 10^{-6}$	0.500	0.1976	0.0037	0.0044	0.0051
0.150	$2.76 \cdot 10^{-6}$	0.600	0.1986	0.0037	0.0052	0.0058
0.150	$2.36 \cdot 10^{-6}$	0.700	0.1947	0.0045	0.0068	0.0069
0.150	$2.07 \cdot 10^{-6}$	0.800	0.2183	0.0097	0.0106	0.0118
0.200	$1.10 \cdot 10^{-5}$	0.200	0.2085	0.0058	0.0072	0.0061
0.200	$8.49 \cdot 10^{-6}$	0.260	0.2286	0.0051	0.0057	0.0045
0.200	$6.69 \cdot 10^{-6}$	0.330	0.2260	0.0046	0.0047	0.0050
0.200	$5.52 \cdot 10^{-6}$	0.400	0.2372	0.0046	0.0057	0.0057
0.200	$4.41 \cdot 10^{-6}$	0.500	0.2399	0.0049	0.0056	0.0055
0.200	$3.68 \cdot 10^{-6}$	0.600	0.2423	0.0057	0.0067	0.0066
0.200	$3.15 \cdot 10^{-6}$	0.700	0.2442	0.0074	0.0066	0.0109
0.250	$3.94 \cdot 10^{-4}$	0.007	0.1950	0.0081	0.0125	0.0078
0.250	$1.84 \cdot 10^{-4}$	0.015	0.2082	0.0083	0.0098	0.0094
0.250	$1.10 \cdot 10^{-4}$	0.025	0.2004	0.0079	0.0086	0.0079
0.250	$5.52 \cdot 10^{-5}$	0.050	0.2289	0.0079	0.0083	0.0080
0.250	$2.30 \cdot 10^{-5}$	0.120	0.2411	0.0034	0.0080	0.0076
0.250	$1.38 \cdot 10^{-5}$	0.200	0.2513	0.0037	0.0056	0.0062
0.250	$1.06 \cdot 10^{-5}$	0.260	0.2676	0.0042	0.0060	0.0064
0.250	$8.36 \cdot 10^{-6}$	0.330	0.2698	0.0048	0.0065	0.0077
0.250	$6.90 \cdot 10^{-6}$	0.400	0.2744	0.0052	0.0054	0.0065
0.250	$5.52 \cdot 10^{-6}$	0.500	0.2848	0.0059	0.0064	0.0073
0.250	$4.60 \cdot 10^{-6}$	0.600	0.2883	0.0071	0.0072	0.0093
0.250	$3.94 \cdot 10^{-6}$	0.700	0.2776	0.0114	0.0105	0.0110

Q^2 (GeV^2)	x	y	F_2	$\pm$ stat	$+$ sys	$-$ sys
0.300	$4.73 \cdot 10^{-4}$	0.007	0.2214	0.0058	0.0047	0.0061
0.300	$2.20 \cdot 10^{-4}$	0.015	0.2169	0.0058	0.0056	0.0056
0.300	$1.32 \cdot 10^{-4}$	0.025	0.2339	0.0061	0.0067	0.0045
0.300	$6.62 \cdot 10^{-5}$	0.050	0.2565	0.0067	0.0052	0.0070
0.300	$2.76 \cdot 10^{-5}$	0.120	0.2700	0.0034	0.0091	0.0091
0.300	$1.65 \cdot 10^{-5}$	0.200	0.2874	0.0042	0.0082	0.0078
0.300	$1.27 \cdot 10^{-5}$	0.260	0.2896	0.0049	0.0063	0.0077
0.300	$1.00 \cdot 10^{-5}$	0.330	0.3253	0.0063	0.0062	0.0089
0.300	$8.28 \cdot 10^{-6}$	0.400	0.3012	0.0064	0.0081	0.0069
0.300	$6.62 \cdot 10^{-6}$	0.500	0.3014	0.0075	0.0058	0.0077
0.300	$5.52 \cdot 10^{-6}$	0.600	0.3221	0.0110	0.0149	0.0118
0.400	$6.31 \cdot 10^{-4}$	0.007	0.2585	0.0071	0.0063	0.0075
0.400	$2.94 \cdot 10^{-4}$	0.015	0.2769	0.0076	0.0067	0.0061
0.400	$1.76 \cdot 10^{-4}$	0.025	0.2869	0.0080	0.0066	0.0082
0.400	$8.83 \cdot 10^{-5}$	0.050	0.3206	0.0087	0.0055	0.0128
0.400	$3.68 \cdot 10^{-5}$	0.120	0.3213	0.0046	0.0098	0.0117
0.400	$2.20 \cdot 10^{-5}$	0.200	0.3369	0.0058	0.0080	0.0085
0.400	$1.70 \cdot 10^{-5}$	0.260	0.3452	0.0070	0.0086	0.0072
0.400	$1.33 \cdot 10^{-5}$	0.330	0.3567	0.0085	0.0095	0.0105
0.400	$1.10 \cdot 10^{-5}$	0.400	0.3594	0.0098	0.0118	0.0083
0.400	$8.83 \cdot 10^{-6}$	0.500	0.3552	0.0137	0.0147	0.0077
0.500	$7.89 \cdot 10^{-4}$	0.007	0.2897	0.0063	0.0058	0.0064
0.500	$3.68 \cdot 10^{-4}$	0.015	0.3020	0.0061	0.0056	0.0064
0.500	$2.20 \cdot 10^{-4}$	0.025	0.3144	0.0060	0.0067	0.0076
0.500	$1.10 \cdot 10^{-4}$	0.050	0.3449	0.0061	0.0064	0.0079
0.500	$4.60 \cdot 10^{-5}$	0.120	0.3599	0.0063	0.0138	0.0132
0.500	$2.76 \cdot 10^{-5}$	0.200	0.3822	0.0082	0.0101	0.0118
0.500	$2.12 \cdot 10^{-5}$	0.260	0.3767	0.0101	0.0103	0.0087
0.500	$1.67 \cdot 10^{-5}$	0.330	0.4265	0.0153	0.0139	0.0125
0.650	$1.02 \cdot 10^{-3}$	0.007	0.3119	0.0074	0.0062	0.0085
0.650	$4.78 \cdot 10^{-4}$	0.015	0.3319	0.0076	0.0083	0.0089
0.650	$2.87 \cdot 10^{-4}$	0.025	0.3559	0.0080	0.0068	0.0092
0.650	$1.43 \cdot 10^{-4}$	0.050	0.3889	0.0087	0.0089	0.0097
0.650	$5.98 \cdot 10^{-5}$	0.120	0.4290	0.0111	0.0193	0.0181
0.650	$3.59 \cdot 10^{-5}$	0.200	0.4971	0.0193	0.0168	0.0297

ZEUS 1997
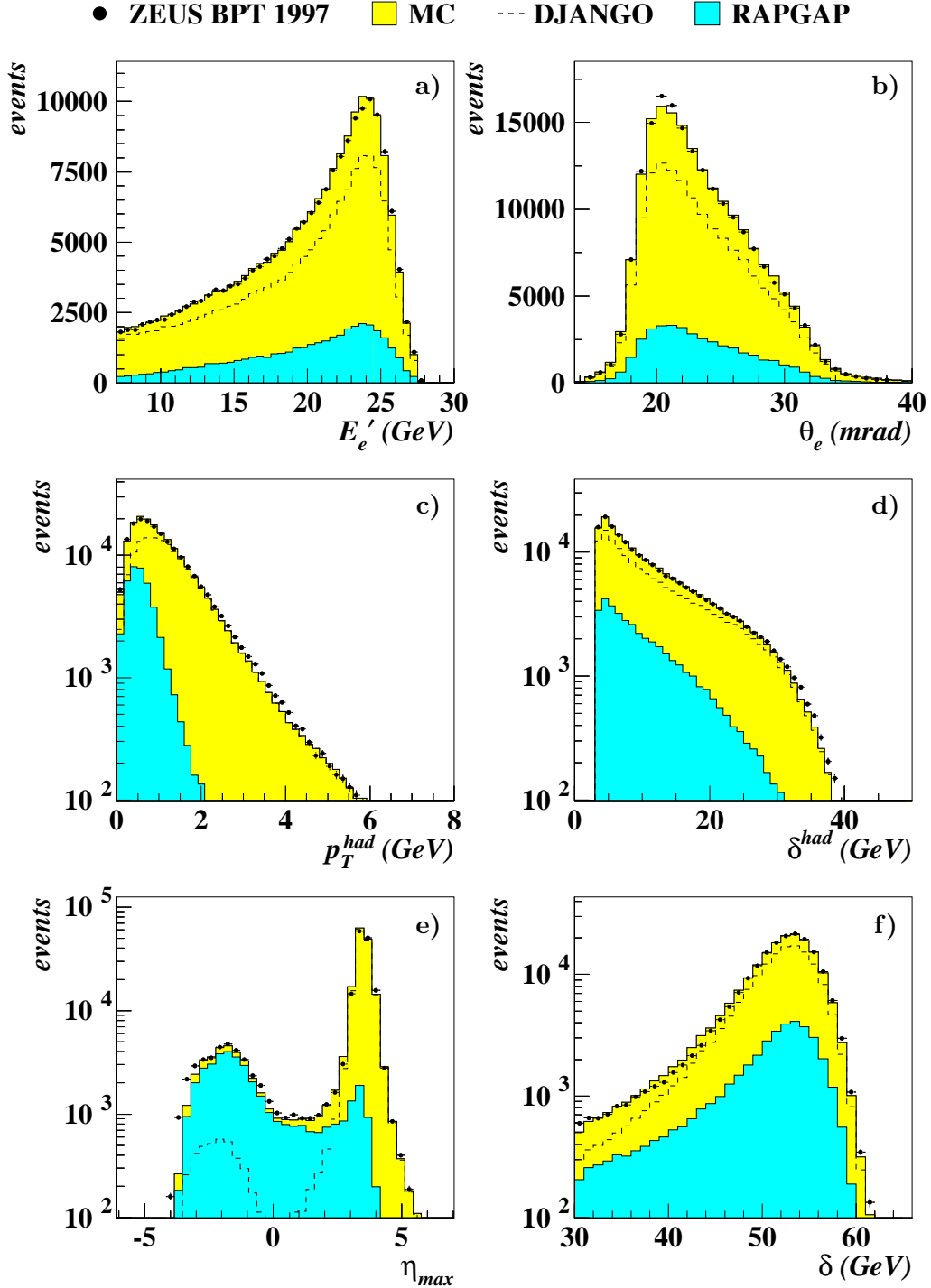
Figure 1: Distributions of reconstructed quantities in data and MC simulation in the region defined by $0.06 < y_{\mathrm{JB}}$ and $y_e < 0.74$: a) energy, E'_e, of the positron measured in the BPC; b) scattering angle, θ_e, of the positron measured in the BPT; c) p_T^{had}; d) δ^{had}; e) η_{max}; f) δ. The points denote measured data, the light shaded histogram is the sum of non-diffractive (DJANGO) and diffractive (RAPGAP) MC, the dark shaded histogram and the dashed line represent the individual contributions from RAPGAP and DJANGO, respectively.

12

ZEUS 1997
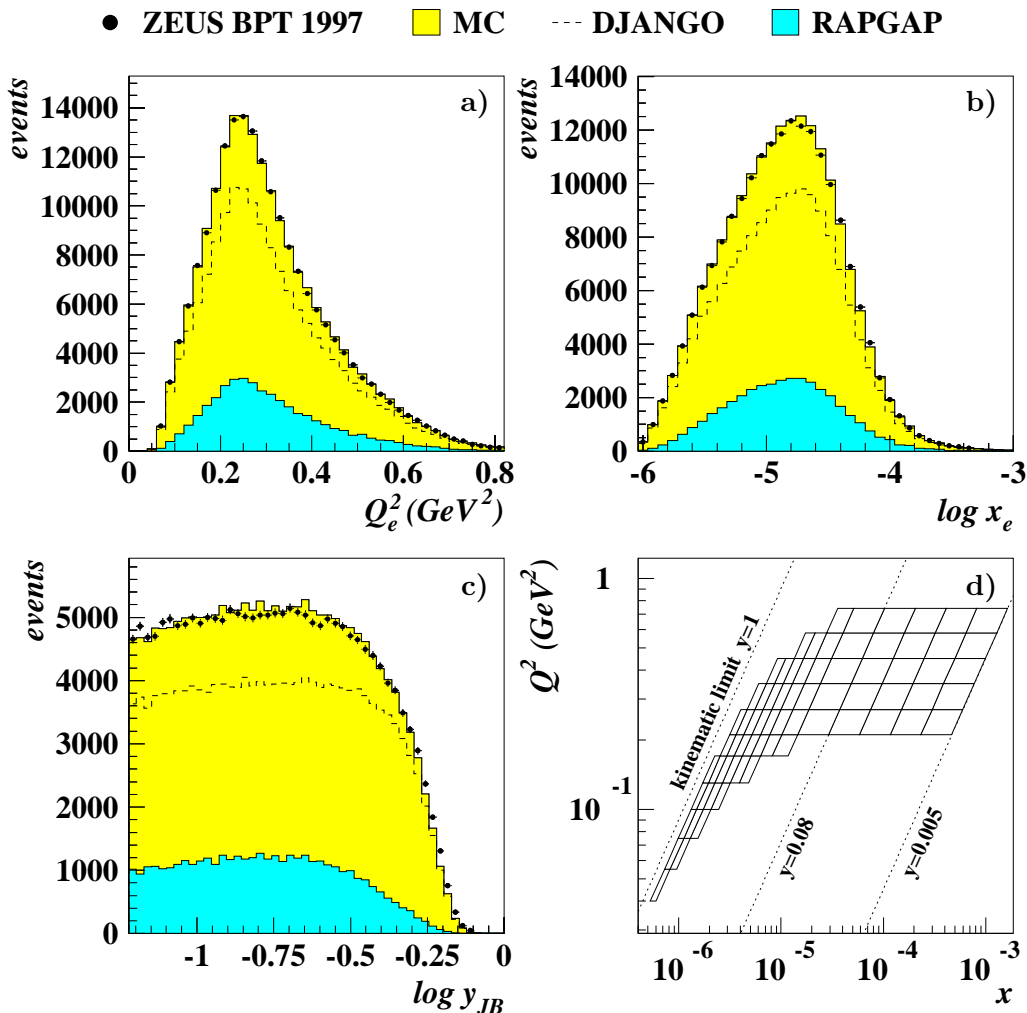
Figure 2: a)–c) Distributions of reconstructed kinematic quantities in data and MC simulation in the region defined by $0.06 < y_{\text{JB}}$ and $y_e < 0.74$: a) Q_e^2; b) x_e; c) y_{JB}. The points denote measured data, the light shaded histogram is the sum of non-diffractive (DJANGO) and diffractive (RAPGAP) MC, the dark shaded histogram and the dashed line represent the individual contributions from RAPGAP and DJANGO, respectively. d) The bins in the kinematic plane (Q^2 vs. x). The bin boundaries in y are 0.005, 0.01, 0.02, 0.04, 0.08, 0.16, 0.23, 0.30, 0.37, 0.45, 0.54, 0.64, 0.74, 0.84; those in Q^2 are 0.040, 0.055, 0.075, 0.10, 0.13, 0.17, 0.21, 0.27, 0.35, 0.45, 0.58, 0.74 GeV^2. The border at $y = 0.08$, above which the electron method and below which the $e\Sigma$ method was used to reconstruct the event kinematics, is also indicated.

13

ZEUS 1997
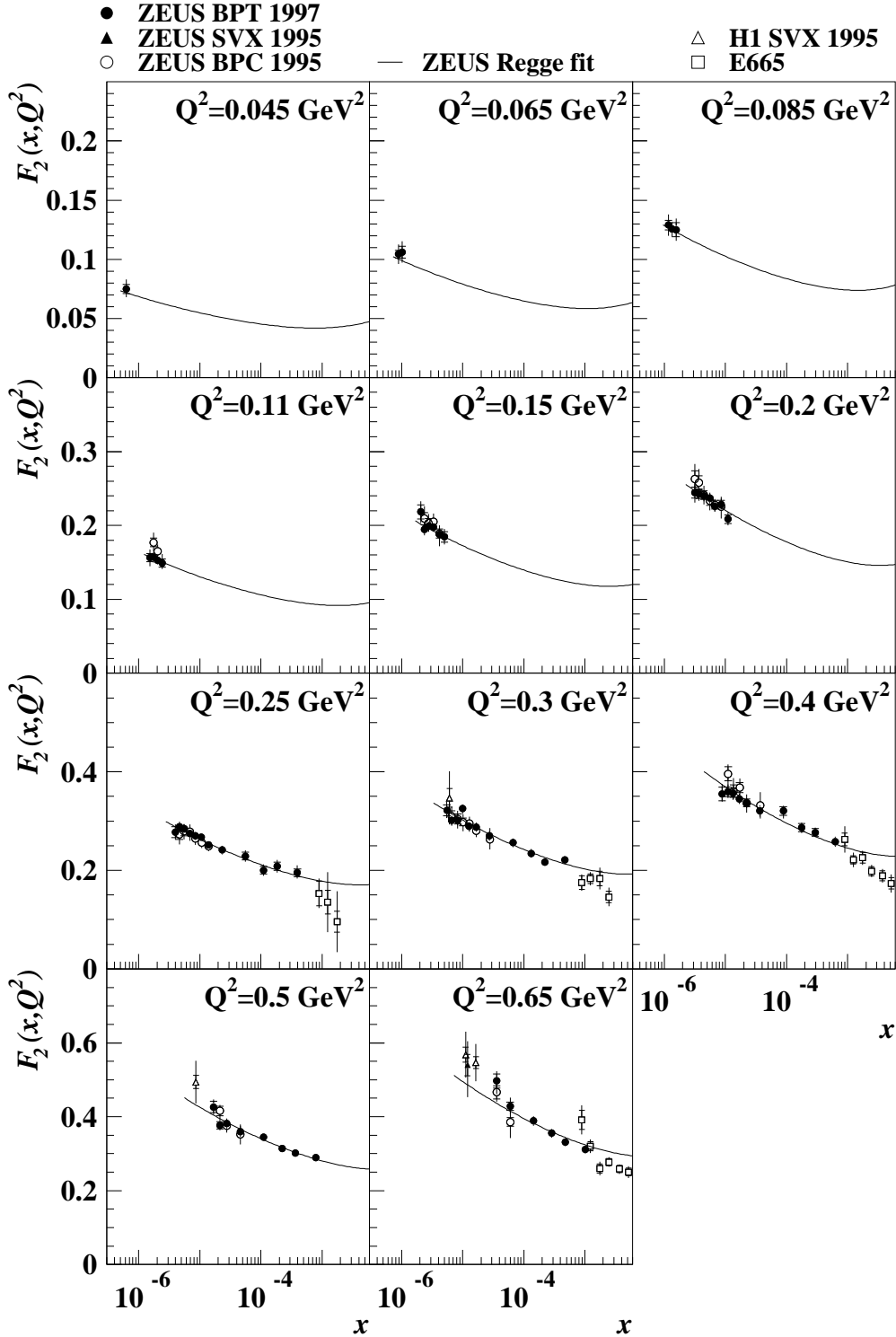
Figure 3: Measured F_2 vs. x in bins of Q^2. The data from the present measurement are indicated by filled circles. The solid line shows the ZEUS Regge fit. Open circles denote the results from a previous analysis, filled and open triangles denote other measurements from ZEUS and H1, respectively, and squares denote results from E665. These other measurements have been shifted to the Q^2 values of the present measurement using the ALLM97 parameterization. The inner error bars represent statistical errors, the outer ones the sum in quadrature of statistical and systematic errors; normalization uncertainties are not included.

ZEUS 1997

- ● **ZEUS BPT 1997**
- ▲ **ZEUS SVX 1995**   --- **ZEUS QCD fit**   △ **H1 SVX 1995**
- ■ **ZEUS 1994**   — **ZEUS Regge fit**   ○ **H1 1994**
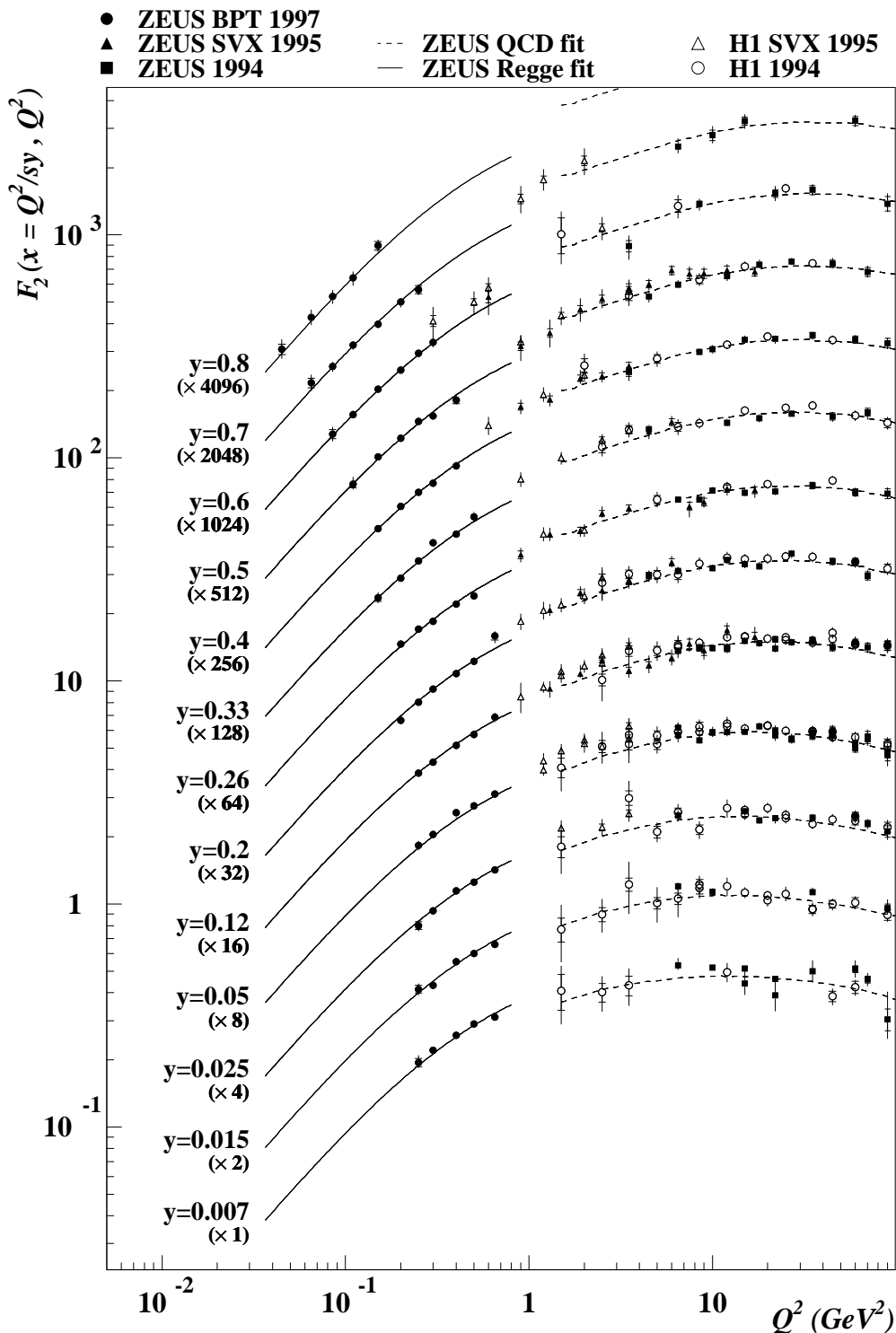
Figure 4: Measured F_2 vs. Q^2 in bins of y. The data from the present measurement are indicated by filled circles. Triangles, filled squares and open circles denote other measurements from ZEUS and H1. The data have been scaled by the numbers in parentheses for clarity of presentation. The solid line at low Q^2 shows the ZEUS Regge fit, the dashed line at higher Q^2 the ZEUS QCD fit. The other measurements have been shifted to the y values of the present measurement using the ALLM97 parameterization.

15

Q^2	y	A−	A+	B−	B+	C−	C+	D−	D+	E	F−	F+	G−	G+	H−	H+	I−	I+	J−	J+	K−	K+	L−	L+	M−	M+	N−	N+	O−	O+
0.045	0.800	−0.8	+3.0	0.0	0.0	−1.6	0.0	−0.7	+0.5	−0.4	+0.3	+2.7	+0.7	+0.4	−0.3	−1.2	−2.1	+0.5	−1.5	+2.1	−1.5	+1.5	−0.7	+0.9	−6.0	+7.8	−2.7	+1.4	+1.5	−1.5
0.065	0.700	0.0	−1.3	0.0	0.0	−0.4	−0.1	−1.4	+0.6	+2.4	+2.1	0.0	−0.5	+0.3	+0.1	+1.6	−0.8	+0.3	−2.5	+3.3	−1.5	+1.5	−2.1	+0.7	−3.7	+3.8	−2.1	+1.1	+2.8	−2.9
0.065	0.800	+1.0	+1.0	0.0	0.0	−1.7	+0.8	−1.2	+0.7	+0.8	+0.7	−2.3	−0.1	+0.1	+0.5	−0.6	+2.3	−0.9	−0.3	+0.7	−1.5	+1.5	−0.9	+0.8	−5.6	+6.3	−2.7	+1.4	+0.5	−0.5
0.085	0.600	+4.2	−0.6	0.0	0.0	−0.7	−0.4	−1.0	+0.7	−2.2	−1.4	−1.0	−0.6	+0.2	+1.2	−0.3	−0.2	−1.4	−1.5	+1.4	−1.5	+1.5	−0.7	0.0	−1.0	+1.0	−1.5	+0.8	+3.2	−3.2
0.085	0.700	+1.5	−0.9	0.0	0.0	−1.2	+0.3	−1.6	+0.8	+0.2	−1.0	+0.6	−0.6	+0.2	+0.6	−0.8	+1.3	−0.7	−0.7	−0.1	−1.5	+1.5	−0.8	+1.0	−2.9	+3.0	−2.1	+1.1	+0.6	−0.6
0.085	0.800	+1.5	0.0	0.0	0.0	−1.1	+1.3	−0.5	+0.7	+0.9	−0.1	+0.2	0.0	−0.1	+0.9	−0.7	+1.1	−1.5	−0.7	0.0	−1.5	+1.5	−1.3	+1.0	−4.8	+5.4	−2.7	+1.4	+0.2	−0.2
0.110	0.500	−0.1	+0.3	+1.4	−0.3	−0.4	+0.3	−1.0	+0.3	+1.3	+3.1	+5.5	−0.3	−0.1	−0.1	−0.5	−0.4	−0.2	−0.8	+0.5	−1.5	+1.5	−0.2	0.0	−0.3	−0.9	+0.5	+2.6	−2.6	
0.110	0.600	+0.4	−0.5	0.0	0.0	−0.4	−0.1	−0.7	+0.5	+0.7	+1.1	+0.1	−0.3	−0.1	+0.9	−0.7	+1.6	−1.0	−0.7	+1.3	−1.5	+1.5	−0.3	+0.5	−1.1	+1.1	−1.5	+0.8	+0.6	−0.7
0.110	0.700	+0.2	−0.4	0.0	0.0	−0.6	+0.2	−0.6	+0.6	+1.5	+0.4	+0.2	−1.0	+0.6	−0.1	−0.3	−0.5	−0.3	−1.5	+0.8	−1.5	+1.5	−0.7	+0.8	−2.3	+2.4	−2.1	+1.1	+0.3	−0.3
0.110	0.800	+0.5	−2.2	0.0	0.0	−0.6	+1.0	−1.7	+0.5	+1.3	+0.1	−0.4	−0.2	+0.3	+1.0	−0.3	+1.0	−0.4	−1.0	+1.4	−1.5	+1.5	−1.8	+1.5	−4.5	+4.9	−2.7	+1.4	+0.1	−0.2
0.150	0.330	0.0	0.0	+0.4	−0.2	+0.1	0.0	+0.3	+0.5	+1.8	−0.6	+1.3	+0.1	+0.4	+0.7	−0.6	+0.2	+0.6	−1.9	−0.6	−1.5	+1.5	−0.5	+0.1	−0.2	+0.2	0.0	0.0	+2.9	−2.9
0.150	0.400	0.0	0.0	+0.5	0.0	−0.3	0.0	−0.5	+0.3	−0.1	+0.1	+1.7	−0.1	+0.2	+1.0	−0.7	+0.5	−0.2	−0.4	+1.1	−1.5	+1.5	−0.1	+0.2	−0.1	+0.1	−0.3	+0.2	+1.1	−1.2
0.150	0.500	+0.1	−0.2	+0.2	−0.3	−0.3	+0.2	−0.3	+0.2	+0.6	+0.6	+0.1	−0.2	−0.6	+0.4	−0.4	+0.1	−0.6	−1.5	+1.5	−1.5	+1.5	−0.3	+0.3	−0.2	+0.2	−0.9	+0.5	+0.5	−0.6
0.150	0.600	+1.1	−1.1	0.0	0.0	−0.3	−0.1	−0.3	+0.5	+0.4	+0.2	+0.2	−0.6	−0.5	+0.3	−0.4	+0.6	−0.1	−0.9	+0.9	−1.5	+1.5	−0.5	+0.6	−0.8	+0.8	−1.5	+0.8	+0.4	−0.4
0.150	0.700	+1.4	−0.4	0.0	0.0	−0.8	+0.3	−0.3	+0.7	0.0	−0.3	+0.2	−0.6	−0.6	+0.6	−0.6	+1.3	−0.5	−0.3	+0.8	−1.5	+1.5	−0.7	+0.8	−1.7	+1.7	−2.1	+1.1	+0.2	−0.2
0.150	0.800	+0.5	−0.7	0.0	0.0	−0.5	+0.7	−0.6	+0.6	−0.5	+0.3	−0.8	−0.1	+0.3	−1.3	−0.7	+0.5	−1.5	+1.5	−1.7	+1.7	−3.6	+4.0	−2.7	+1.4	+0.1	−0.1				
0.200	0.200	0.0	0.0	+0.5	−0.2	0.0	0.0	+0.4	0.0	0.0	−0.6	+1.1	−0.4	−0.2	+1.1	−0.7	−0.1	+0.7	−0.2	+1.2	−1.5	+1.5	−0.4	+0.2	−0.3	+0.3	0.0	0.0	+2.1	−2.2
0.200	0.260	0.0	0.0	+0.3	+0.1	0.0	0.0	+0.1	−0.1	+1.1	+0.1	−0.4	0.0	−0.2	+1.3	−0.7	+0.3	+0.2	−0.4	+0.5	−1.5	+1.5	−0.3	+0.2	0.0	0.0	0.0	0.0	+0.8	−0.8
0.200	0.330	0.0	0.0	0.0	−0.3	0.0	0.0	−0.2	−0.2	−0.2	+0.8	−0.5	−0.5	−0.2	+0.8	−1.0	+0.4	−0.8	−0.2	+0.7	−1.5	+1.5	−0.2	+0.1	−0.1	+0.1	0.0	0.0	+0.4	−0.4
0.200	0.400	0.0	0.0	−0.3	−0.1	−0.1	+0.1	+0.2	+0.8	−0.2	−0.1	−0.3	−1.2	+1.1	−0.8	+1.0	−0.2	−0.9	+0.4	−1.5	+1.5	−0.3	+0.3	−0.3	+0.3	−0.3	+0.2	+0.3	−0.4	
0.200	0.500	+0.3	−0.3	+0.4	+0.2	−0.1	0.0	−0.3	0.0	+0.3	+0.3	0.0	−0.4	−0.6	+0.8	−0.7	+0.7	−0.6	−0.6	+1.1	−1.5	+1.5	−0.2	+0.3	−0.1	+0.2	−0.9	+0.5	+0.4	−0.3
0.200	0.600	+0.5	0.0	0.0	0.0	−0.3	0.0	−0.6	+0.4	+0.5	0.0	0.0	−0.9	−0.7	+1.0	−0.3	+1.6	−0.6	−0.4	+0.7	−1.5	+1.5	−0.4	+0.2	−0.5	+0.5	−1.5	+0.8	+0.2	−0.2
0.200	0.700	+0.1	−0.3	0.0	0.0	−0.5	0.0	−1.4	+0.6	+0.3	−0.2	0.0	−1.2	−0.8	+0.6	−0.9	+0.7	−2.5	−0.6	+0.2	−1.5	+1.5	−0.5	+0.6	−1.5	+1.5	−2.1	+1.1	+0.1	−0.1
0.250	0.007	0.0	0.0	−0.2	−1.0	−0.1	−0.1	−0.2	−0.1	−0.5	+0.7	+5.1	−0.7	−0.2	+1.8	−2.0	0.0	+0.3	−0.9	+2.6	−1.5	+1.5	−2.0	−0.3	−0.2	+0.2	0.0	0.0	+1.5	−1.6
0.250	0.015	0.0	0.0	0.0	0.0	+0.1	0.0	+0.1	−0.2	−3.3	+2.6	+0.2	−0.4	+0.4	+2.3	−2.3	−0.1	+0.1	−0.1	−0.1	−1.5	+1.5	+2.1	+0.9	−0.2	+0.3	0.0	0.0	+1.4	−1.4
0.250	0.025	0.0	0.0	0.0	0.0	+0.1	−0.1	−0.8	0.0	+3.6	+1.3	−0.5	+0.2	+0.6	−2.7	0.0	−1.1	−0.6	−1.3	−1.5	+1.5	−0.6	−0.7	−0.1	+0.2	0.0	0.0	+1.1	−1.2	
0.250	0.050	0.0	0.0	0.0	0.0	+0.1	+0.4	+0.3	−0.5	+1.3	0.0	−0.7	+0.1	+1.4	−1.5	+0.1	−0.4	−2.4	+2.1	−1.5	+1.5	+1.3	−0.8	+0.3	−0.3	0.0	0.0	+0.7	−0.7	
0.250	0.120	0.0	0.0	−0.2	+0.9	0.0	0.0	0.0	0.0	0.0	−0.2	+1.4	−0.2	−0.2	−0.2	−0.9	+0.7	−1.0	+0.5	−1.5	+1.5	−2.3	+2.3	−0.1	+0.1	0.0	0.0	+0.2	−0.2	
0.250	0.200	0.0	0.0	−0.2	+0.2	0.0	0.0	+0.2	−0.1	+0.4	+0.2	−0.5	−0.7	−0.4	+1.1	−1.3	−0.3	−0.2	−0.8	+1.0	−1.5	+1.5	−0.4	+0.3	0.0	0.0	0.0	0.0	+0.1	−0.1
0.250	0.260	0.0	0.0	+0.3	−0.2	0.0	0.0	+0.1	+0.1	+0.2	−0.2	−0.2	−0.9	−1.0	+0.2	−0.2	−1.2	+1.2	−1.5	+1.5	−0.3	+0.3	−0.1	+0.1	0.0	0.0	+0.1	−0.1		
0.250	0.330	0.0	0.0	+0.5	−0.4	0.0	0.0	+0.1	0.0	+0.3	+0.4	−0.6	−0.7	−1.8	+1.5	−0.9	+0.7	−0.3	−0.7	+0.6	−1.5	+1.5	−0.2	+0.3	0.0	0.0	0.0	0.0	+0.1	−0.2
0.250	0.400	0.0	0.0	+0.3	+0.2	0.0	0.0	+0.1	0.0	+0.6	+0.5	−0.4	−0.4	−0.7	+0.4	−1.0	+0.4	−0.7	−0.8	+0.7	−1.5	+1.5	−0.2	+0.2	−0.1	+0.1	−0.3	+0.2	+0.2	−0.3
0.250	0.500	0.0	0.0	−0.3	+0.1	+0.1	+0.1	−0.2	0.0	+0.4	+1.3	+0.3	−0.1	−1.0	−1.0	−0.1	−0.4	+0.4	−0.9	−0.7	+0.5	−1.5	+1.5	−0.2	+0.2	0.0	0.0	−0.9	+0.5	+0.2	−0.3
0.250	0.600	−0.2	0.0	0.0	0.0	−0.1	−0.2	−0.9	+0.3	+1.4	0.0	+0.4	+0.1	−1.2	+0.6	−0.9	+0.3	−0.8	−1.4	+0.4	−1.5	+1.5	−0.1	+0.2	−0.6	+0.7	−1.5	+0.8	+0.1	−0.1
0.250	0.700	+1.5	+0.1	0.0	0.0	−0.3	−0.8	−0.4	+0.9	+0.2	−1.6	−1.4	+0.7	−1.4	+0.1	+0.1	+0.7	+0.3	+0.1	+2.1	−1.5	+1.5	−0.9	+1.0	−1.3	+1.4	−2.1	+1.1	+0.1	−0.1
0.300	0.007	0.0	0.0	0.0	−1.0	0.0	−0.1	0.0	0.0	−0.5	+0.4	−0.1	−0.4	−0.6	+0.6	−0.7	−0.1	−0.2	−0.9	+0.6	−1.5	+1.5	−1.4	+1.1	−0.2	+0.2	0.0	0.0	0.0	−0.1
0.300	0.015	0.0	0.0	0.0	0.0	0.0	0.0	+0.7	+0.2	+1.1	+0.1	+0.9	−0.5	−0.7	−0.4	−0.3	0.0	0.0	−1.8	+1.1	−1.5	+1.5	+0.5	+0.6	−0.2	+0.2	0.0	0.0	0.0	0.0
0.300	0.025	0.0	0.0	0.0	0.0	+0.1	0.0	+0.4	0.0	+0.4	+1.1	−0.1	−1.0	+0.7	0.0	+0.2	+0.1	+0.3	+1.9	−1.5	+1.5	−0.6	−0.3	0.0	0.0	0.0	0.0	0.0	0.0	
0.300	0.050	0.0	0.0	0.0	0.0	0.0	0.0	−0.4	0.0	−0.3	−1.1	−0.2	−0.4	−1.7	+0.3	+0.4	−0.1	+0.3	−0.6	+1.2	−1.5	+1.5	+0.2	−0.3	+0.1	−0.2	0.0	0.0	0.0	0.0
0.300	0.120	0.0	0.0	+0.5	+0.4	0.0	0.0	+0.1	0.0	−0.1	−0.2	−0.2	−0.8	−1.1	−0.4	+0.1	−1.1	+1.1	−1.0	+1.2	−1.5	+1.5	−2.2	+2.5	0.0	−0.1	0.0	0.0	0.0	0.0
0.300	0.200	0.0	0.0	+0.1	0.0	0.0	0.0	+0.1	+0.1	+0.6	+0.3	−0.2	−0.4	−1.7	+2.0	−1.1	+0.8	0.0	−0.7	+0.6	−1.5	+1.5	−0.4	+0.3	−0.1	+0.1	0.0	0.0	0.0	0.0
0.300	0.260	0.0	0.0	+0.2	−0.1	+0.1	0.0	−0.1	−0.1	+0.8	+0.2	−0.1	−1.2	−0.8	+0.9	−1.4	0.0	0.0	−0.3	−0.6	+0.9	−1.5	+1.5	−0.2	+0.2	−0.1	+0.1	0.0	0.0	0.0
0.300	0.330	0.0	0.0	+0.3	−0.2	+0.2	0.0	+0.2	+0.1	+0.6	+0.1	−0.1	−1.2	−1.3	0.0	−1.0	+0.1	−0.7	−0.9	+0.8	−1.5	+1.5	−0.2	+0.3	−0.1	+0.1	0.0	0.0	0.0	0.0
0.300	0.400	0.0	0.0	+0.1	−0.4	+0.2	0.0	−0.2	+0.1	+0.7	+0.1	+0.1	−0.7	−0.7	+1.5	−0.7	+1.0	−0.1	−1.1	+1.2	−1.5	+1.5	−0.2	+0.1	−0.1	+0.1	−0.3	+0.2	+0.1	−0.1
0.300	0.500	0.0	+0.1	+0.5	+0.3	0.0	0.0	−0.2	−0.5	+0.2	+0.4	−0.6	−0.2	−0.2	−0.1	−0.6	−0.3	−1.3	+0.8	−1.5	+1.5	−0.3	+0.3	−0.2	+0.3	−0.9	+0.5	+0.1	−0.1	
0.300	0.600	−1.4	−0.4	0.0	0.0	+0.5	+0.2	−0.3	0.0	+3.4	−1.1	−0.2	+0.3	−2.4	+1.6	−0.3	+1.2	−0.3	+0.2	+1.7	−1.5	+1.5	−0.3	+0.2	−0.5	+0.7	−1.5	+0.8	+0.1	−0.1
0.400	0.007	0.0	0.0	0.0	+0.7	0.0	0.0	−0.5	+0.2	+1.5	+0.5	0.0	−0.7	−1.5	−0.9	0.0	−0.3	+0.1	−1.2	+0.8	−1.5	+1.5	−0.7	0.0	−0.2	+0.3	0.0	0.0	0.0	0.0
0.400	0.015	0.0	0.0	0.0	0.0	0.0	0.0	+0.1	−0.1	+0.7	0.0	0.0	−0.2	−1.4	+0.3	+0.8	0.0	0.0	−0.4	−1.2	−1.5	+1.5	+0.3	+0.9	−0.1	+0.1	0.0	0.0	0.0	0.0
0.400	0.025	0.0	0.0	0.0	0.0	+0.1	0.0	−0.2	−0.2	+1.1	+0.2	−0.1	−1.5	−1.7	−0.4	0.0	0.0	−0.1	−0.8	+1.1	−1.5	+1.5	+0.8	+0.1	0.0	+0.1	0.0	0.0	0.0	0.0
0.400	0.050	0.0	0.0	0.0	0.0	0.0	−0.1	+0.1	−0.2	+0.7	+0.1	−0.2	−2.0	−2.0	−0.5	−0.9	+0.1	+0.4	−1.2	−0.2	−1.5	+1.5	−1.6	−0.7	+0.2	−0.2	0.0	0.0	0.0	0.0
0.400	0.120	0.0	0.0	+0.2	+0.3	0.0	0.0	+0.3	0.0	−0.1	−0.4	−1.5	0.0	−0.4	−1.0	+0.7	−0.8	+0.4	−1.2	+1.3	−1.5	+1.5	−2.6	+2.5	0.0	0.0	0.0	0.0	0.0	0.0
0.400	0.200	0.0	0.0	−0.4	+0.7	+0.1	−0.1	+0.3	−0.1	+0.9	−0.1	−0.1	−0.9	−1.3	+0.6	−0.8	−0.6	+0.4	−0.7	+1.1	−1.5	+1.5	−0.3	+0.4	+0.2	−0.1	0.0	0.0	0.0	0.0
0.400	0.260	0.0	0.0	+0.1	−0.2	0.0	+0.1	+0.1	0.0	+1.1	0.0	0.0	−0.5	−0.9	+1.1	−0.4	+0.5	+0.3	−1.0	+1.2	−1.5	+1.5	−0.1	+0.2	−0.1	+0.1	0.0	0.0	0.0	0.0
0.400	0.330	0.0	0.0	+0.5	−0.5	−0.1	−0.1	+0.3	+0.1	+1.9	+0.1	−0.2	−0.8	−1.7	+0.3	−0.7	−0.9	0.0	−1.3	+1.0	−1.5	+1.5	−0.3	+0.3	+0.2	−0.2	0.0	0.0	0.0	0.0
0.400	0.400	0.0	0.0	+0.5	+0.3	+0.2	−0.1	−0.1	+0.1	+2.1	+0.4	−0.3	+0.1	−0.9	+1.3	−1.2	+1.4	−0.9	−0.3	+0.6	−1.5	+1.5	−0.2	0.0	−0.2	+0.3	−0.3	+0.2		
0.400	0.500	−0.5	+0.4	−0.5	−0.2	+0.6	+0.1	−0.7	+0.1	+2.7	+0.9	+0.2	+0.6	−0.8	+1.4	−0.1	+1.5	+0.8	+1.1	+0.3	−1.5	+1.5	−0.1	+0.1	−0.2	+0.3	−0.9	+0.5	0.0	0.0
0.500	0.007	0.0	0.0	0.0	−0.2	0.0	−0.1	+0.2	−0.1	−0.3	0.0	+0.1	−0.5	−0.7	+0.9	−0.8	0.0	+0.1	−0.9	+0.7	−1.5	+1.5	−0.5	+0.4	−0.1	+0.2	0.0	0.0	0.0	0.0
0.500	0.015	0.0	0.0	0.0	0.0	0.0	−0.1	−0.4	−0.1	+0.1	0.0	−0.6	+0.6	−0.9	+0.1	+0.1	−1.0	+0.7	−1.5	+1.5	+0.2	+0.5	−0.2	+0.2	0.0	0.0	0.0	0.0		
0.500	0.025	0.0	0.0	0.0	+0.1	0.0	+0.4	0.0	−0.3	0.0	+0.2	−0.9	−1.0	+0.3	−0.2	−0.1	+0.2	−0.8	+1.4	−1.5	+1.5	0.0	−1.0	−0.2	+0.2	0.0	0.0	0.0	0.0	
0.500	0.050	0.0	0.0	0.0	+0.1	0.0	+0.1	0.0	+0.1	−0.6	−1.0	+0.2	−0.5	−0.2	+0.1	−1.1	+0.9	−1.5	+1.5	+0.4	+0.1	−0.2	−0.2	0.0	0.0	0.0	0.0			
0.500	0.120	0.0	0.0	−0.4	−1.3	+0.1	0.0	+0.3	−0.1	+1.4	0.0	+0.1	−1.0	−1.8	+0.5	+0.7	−0.7	+1.3	−0.6	+1.1	−1.5	+1.5	−2.1	+2.6	−0.1	+0.1	0.0	0.0	0.0	0.0
0.500	0.200	0.0	0.0	+0.1	+0.5	0.0	0.0	0.0	−0.1	+1.7	−0.2	0.0	−0.9	−1.6	+1.0	−1.5	−0.2	−0.3	−1.1	+0.7	−1.5	+1.5	−0.5	+0.3	−0.2	+0.3	0.0	0.0	0.0	0.0
0.500	0.260	0.0	0.0	−0.1	+0.1	0.0	+0.7	−0.1	+1.7	+0.9	−0.4	−0.2	−1.0	+0.1	−1.3	+0.2	−0.2	−0.4	0.0	−1.5	+1.5	−0.2	+0.2	−0.1	+0.1	0.0	0.0	0.0	0.0	
0.500	0.330	0.0	0.0	−0.4	+0.4	−0.1	−0.1	−0.2	−0.1	+2.6	−0.4	−1.7	+0.5	−1.1	+0.9	−1.0	+0.6	−1.0	+0.4	+0.1	−1.5	+1.5	−0.2	0.0	−0.1	+0.1	0.0	0.0	0.0	0.0
0.650	0.007	0.0	0.0	0.0	−0.4	0.0	+0.1	0.0	0.0	−0.2	−0.7	+0.2	−0.2	−1.8	−0.8	+0.8	−0.1	0.0	−0.7	+0.8	−1.5	+1.5	−0.2	+0.2	−0.4	+0.4	0.0	0.0	0.0	0.0
0.650	0.015	0.0	0.0	0.0	+0.1	0.0	+0.4	−0.1	+0.2	−0.7	−0.2	−0.4	−1.7	−0.7	+1.2	−0.1	+0.2	−0.9	+1.2	−1.5	+1.5	+0.4	+0.9	−0.2	+0.2	0.0	0.0	0.0	0.0	
0.650	0.025	0.0	0.0	0.0	+0.1	0.0	+0.3	−0.1	+0.1	+0.7	+0.2	0.0	−1.7	−0.9	+0.6	−0.3	+0.1	−0.4	+0.4	−1.5	+1.5	−0.8	+0.3	−0.2	+0.2	0.0	0.0	0.0	0.0	
0.650	0.050	0.0	0.0	0.0	+0.1	0.0	+0.1	−0.2	+0.4	+1.0	−0.7	+0.1	−0.9	−1.2	+1.1	−0.4	+0.3	−0.9	+0.7	−1.5	+1.5	−0.4	0.0	+0.2	−0.3	0.0	0.0	0.0	0.0	
0.650	0.120	0.0	0.0	−1.6	−0.5	+0.2	0.0	+0.2	−0.1	+3.2	+0.9	−0.8	+0.7	−1.8	−0.8	+0.1	−1.3	+0.6	−0.3	0.0	−1.5	+1.5	−2.6	+2.5	−0.1	+0.1	0.0	0.0	0.0	0.0
0.650	0.200	0.0	0.0	−1.3	−0.8	−0.1	−0.1	−0.5	+0.2	+2.2	+0.4	−4.9	+0.4	−1.2	+1.9	−2.3	+0.6	−0.1	+0.3	−0.6	−1.5	+1.5	−0.5	+0.2	−0.1	+0.2	0.0	0.0	0.0	0.0

Table 2: Individual effects on F_2 of each of the systematic checks described in Section 5.4 (in percent). The letters denote variations of: A) δ cut; B) y_{JB} cut; C) BPC shower width cut; D) BPC/BPT track match cut; E) BPT vertex cut; F) fiducial area cut in X; G) fiducial area cut in Y; H) BPC energy scale; I) BPC energy linearity; J) BPC/BPT alignment; K) BPT efficiency; L) CAL energy scale; M) BPT energy scale; N) background normalization; O) radiative corrections.